EES Batteries

ROYAL SOCIETY OF CHEMISTRY

PAPER

View Article Online
View Journal

Cite this: DOI: 10.1039/d5eb00037h

Enabling fast formation for lithium-ion batteries with a localized high-concentration electrolyte†

Seamus Ober and Arumugam Manthiram *

Formation cycling currently represents a severe bottleneck in the lithium-ion battery (LIB) manufacturing process. The low currents required to form a stable solid-electrolyte interphase (SEI) and avoid lithium plating lead to long formation times. Consequently, formation represents one of the most expensive and energy-intensive stages of LIB production, and one of the largest opportunities for reducing production costs. Herein, we investigate the impacts of increasing the formation rate on graphite anode with different electrolytes and electrode loading conditions. We find that although LIBs are tolerant of formation rates up to ~1C at ~2.2 mA h cm^{-2} loading, lithium plating leads to severe loss of lithium inventory when the loading is increased to a practical value of ~5.0 mA h cm^{-2}, leading to low specific capacity. However, by introducing a localized high-concentration electrolyte, this effect can be effectively mitigated, enabling a first-cycle duration of 2–3 h with minimal loss of capacity even at practical anode loading.

Received 21st February 2025,
Accepted 23rd May 2025

DOI: 10.1039/d5eb00037h

rsc.li/EESBatteries

Broader context

Lithium-ion batteries (LIBs) have become one of the most pervasive technologies of the modern era. Since their commercialization, they have been used extensively for small-scale applications, such as portable electronic devices. In recent years, the growing electric mobility sector and other large-scale applications have placed tremendous demand on LIB manufacturers to increase production throughput. Of the many steps of LIB manufacturing, one of the most costly and time-consuming is formation cycling, during which assembled LIBs are subjected to a series of slow charge–discharge cycles over days or weeks before final testing. Although formation cycling is critical to the safety and performance of LIBs, the duration of typical formation cycling procedures presents a severe bottleneck in the LIB production process. Consequently, shortening the formation process is a promising strategy to reduce the cost and increase the throughput rate of LIB production, provided it does not compromise the cell performance or safety. In our work, we demonstrate an electrolyte engineering strategy which enables the formation cycle duration of LIBs with practical design parameters to be reduced to 2–3 hours with minimal impacts to long-term cell performance. This novel approach introduces an applicable pathway to reducing formation cost and time.

Introduction

Since their commercialization in 1991, lithium-ion batteries (LIBs) have paved the road for rapid technological advancements, proving instrumental in bringing about profound changes to the contemporary human experience at a global scale. Tremendous investments in R&D and large-scale manufacturing facilities have continuously driven down the cost of LIB production,[1,2] in spite of fluctuating raw material prices. In turn, the decreasing price of LIBs has accelerated their impact, enabling the proliferation of large-scale technological applications, such as electric vehicles (EVs) and grid-scale storage systems. To meet the anticipated growth in demand for LIBs in the coming years and decades, it is critical to accelerate the rate of LIB production and further reduce the cost.[3]

The LIB cell manufacturing process consists of several main stages, including electrode coating and drying, electrode stack wrapping, electrolyte injection, formation cycles/resting, and quality control inspection processes.[4,5] Of these stages, formation cycling is one of the most expensive, energy-intensive, and time-consuming, presenting a large production bottleneck.[4,6] While specific estimates of the proportion of production cost and energy investment incurred by cell formation vary widely,[4] it is clear that a reduction in formation time or energy investment would represent a significant improvement in throughput and cost savings for LIB manufacturers.[7] For example, a recent study calculated that accelerated formation represents the third-largest potential cost savings of any single production parameter for reducing LIB manufacturing cost, behind (second) increasing the nickel content of the layered cathode material or (first) increasing the electrode thickness.[8] Notably, these latter options would necessarily

Materials Science and Engineering Program and Texas Materials Institute, The University of Texas at Austin, Austin, Texas 78712, USA.
E-mail: manth@austin.utexas.edu

† Electronic supplementary information (ESI) available. See DOI: https://doi.org/10.1039/d5eb00037h

compromise cell performance with regard to stability and rate capability.

Although industrial formation cycling protocols vary between manufacturers and are largely proprietary, most recent analyses suggest they generally consist of slow (*e.g.*, C/20 and/or C/10 rate) cycles and wetting/degassing steps carried out at elevated temperatures, generally lasting several days to weeks.[8–11] Consequently, large dedicated factory floor spaces and battery cyclers are required to accommodate them, and the process is generally energy-intensive.[11] Even at a small lab scale (*e.g.*, for materials researchers), formation cycling generally presents a significant waiting period which constrains experimental throughput.

The propensity for lithium–metal plating on the graphite anode remains the key constraint to reducing formation time.[10] During charging at high rates and/or high states of charge (SOC), the graphite anode potential falls below that of Li/Li^+, and the deposition of lithium metal becomes thermodynamically favorable over lithium intercalation into graphite. Consequently, lithium ions (Li^+) are reduced to lithium metal (Li^0) and deposited onto graphite surface.[12] Due to its tendency to deposit in dendritic morphologies, especially under high current density, lithium deposits can pierce the separator and internally short-circuit the cell, posing a substantial safety risk.[13,14] Additionally, the high reactivity of lithium metal, combined with its high surface area on deposition, causes it to continuously form thick passivating layers during cycling. This can lead to a loss of electrical contact with the anode, rendering the deposited lithium electrochemically inaccessible (*i.e.*, "dead Li").[15,16] Integration of lithium in the solid-electrolyte interphase (SEI) itself, such as lithium oxide, fluoride, carbonate, and alkoxide species, can also contribute significantly to lithium inventory loss.[17]

Despite the clear need for fast formation cycling strategies, there are relatively few studies addressing this topic, even fewer of which were published recently. An *et al.*[18] and Lee *et al.*[19] both proposed restricting the potential or SOC cutoff during formation, interestingly focusing on opposite operating potential regimes. In this approach, particular consideration must be given to the cathode side, for which reaching high potentials is critical to achieve high reversible capacity.[20] Mao *et al.* studied the impacts of increased formation C-rates and reduced number of cycles.[21] Heimes *et al.* investigated the roles of applied pressure and temperature in reducing formation time in large-format pouch cells.[22] Drees *et al.* applied a strategic formation current profile based on an electrode equivalent-circuit model to minimize the formation time, achieving a formation time <1 h.[23]

The effect of various formation current–potential protocols on SEI formation has also been studied. In general, it is found that fast formation may lead to more facile lithium transport characteristics in the SEI,[24,25] leading to superior electrochemical performance,[18,19] provided it does not incur severe lithium inventory loss *via* plating. Among the aforementioned studies,[18,19,21–25] the various strategies to reduce formation time did not lead to any significant loss of electrochemical performance. The reported graphite electrode loading ranges from 6.4 mg cm^{-2} (An *et al.*)[18] to 8.55 mg cm^{-2} (Oh *et al.*),[24] which (we estimate) corresponds to a range of ~2.2–3.0 mA h cm^{-2}. This is significantly lower than the loading required to meet the energy density targets for some applications of practical LIBs, as will be addressed in detail later. In a more recent study by Drees *et al.*, a 3-electrode cell was used to directly control the graphite anode potential during formation in order to prevent lithium plating, enabling a formation time of <2 h and improved electrochemical performance with 4.13 mA h cm^{-2} graphite electrode loading.[26] Although the addition of a reference electrode to control the graphite potential is impractical for scalable production of LIBs, this work clearly demonstrated that formation time can be reduced dramatically when lithium plating is suppressed.

The large research effort toward developing advanced LIB electrolytes in recent years has led to significant advancements in our understanding of SEI formation and electrolyte design strategies for controlling it.[27,28] However, despite the progress in electrolyte design and fast formation techniques, to the best of our knowledge there has been no investigation of electrolyte engineering strategies for enabling faster formation. In this study, we explore the limits of formation cycle rates in LIB full cells. Although the $LiNi_{0.80}Mn_{0.10}Co_{0.10}O_2$ (NMC811) cathode does not suffer irreversible capacity loss resulting from fast formation rates, the loss of lithium inventory due to lithium plating on the graphite anode limits the achievable formation rate in full cells. To circumvent this problem, we employ a localized high-concentration electrolyte (LHCE) based on lithium bis(fluorosulfonyl)imide (LiFSI) salt, which was previously shown to suppress irreversible lithium plating.[29,30] We demonstrate that for a conventional electrolyte, the maximum formation rate which can be achieved without capacity loss depends strongly on the thickness and ion-transport capability within the porous electrode. This suggests that some previous studies, which used low or medium electrode loading, may not translate well to practical cells with high loading. However, the LHCE used here minimizes lithium inventory loss, allowing fast formation even with thick electrodes, with minimal loss of capacity. This result is attributed to the formation of an anode SEI that offers facile charge-transfer between the electrolyte and electrode.

Experimental section

Materials preparation

$Ni_{0.8}Mn_{0.1}Co_{0.1}(OH)_2$ was prepared by hydroxide coprecipitation. Briefly, aqueous solutions of $NiSO_4{\cdot}6H_2O$ (Chemsavers, 99.9%), $MnSO_4{\cdot}H_2O$ (Acros Organics, 99%), and $CoSO_4{\cdot}7H_2O$ (Alfa Aesar, 98%) and KOH (Fisher, 85%) were pumped at controlled rates into a reaction solution containing aqueous NH_4OH (Fisher) as a chelating agent in a continuously stirred tank reactor. The pH and temperature were maintained at, respectively, 11.5 and 50 °C during the reaction. The recovered product was washed several times with deionized water and

dried for several days. To synthesize $LiNi_{0.8}Mn_{0.1}Co_{0.1}O_2$ (NMC811), $Ni_{0.8}Mn_{0.1}Co_{0.1}(OH)_2$ was mixed together with pre-ground $LiOH{\cdot}H_2O$ (Alfa Aesar, 98%) in 3 mol% excess. The mixture was transferred to an alumina crucible and calcined in a tube furnace at 770 °C for 12 h under oxygen flow at 1.0 ft^3 h^{-1} flow rate. After calcination, the material was stored in an argon-filled glovebox until use.

Electrolytes were prepared inside an argon-filled glovebox. The standard electrolyte was prepared by dissolving 1.0 M $LiPF_6$ in a solvent mixture composed of 30 wt% ethylene carbonate (EC, Sigma) and 70 wt% ethyl methyl carbonate (EMC, Gotion) with 2 wt% vinylene carbonate (VC, Gotion) added, labeled as LP57. A second electrolyte was prepared by dissolving 1.5 M lithium bis(fluorosulfonyl)imide (LiFSI, Gotion) in a solvent mixture consisting of fluoroethylene carbonate (FEC, Sigma), dimethyl carbonate (DMC, Sigma) and 1,1,2,2 tetrafluoropropyl-2,2,2 trifluoroethyl ether (TTEE, Synquest) in a 1 : 19 : 27.4 mass ratio, labeled as LHCE, as described in our previous work.[29] The electrolytes were stored in polyethylene vials in an argon-filled glovebox.

Electrode preparation

Cathode slurries were prepared by dispersing NMC811, polyvinylidene fluoride (PVDF, Arkema) polymer binder, and carbon black in *N*-methyl pyrrolidone (NMP, Sigma) in a high-shear mixer (Thinky) at 2000 rpm for several minutes. A doctor blade was then used to coat the dispersion evenly on double-sided carbon-coated aluminum foil. To achieve nominal loading of ~2.1 mA h cm^{-2} (11.7 mg cm^{-2}), NMC811 : PVDF : carbon were combined in a weight ratio of 90 : 5 : 5. To achieve nominal loading of ~4.5 mA h cm^{-2} (26.1 mg cm^{-2}), this ratio was adjusted to 95 : 2.5 : 2.5 and the doctor blade height was increased to yield a thicker electrode. After casting, the electrodes were dried for ~30 minutes in air at 110 °C before transferring to vacuum oven at 110 °C. After thoroughly drying, the cathodes were pressed in a heated calender at 110 °C to a density ~3.2 g cm^{-3}. For coin cells, metal punches were used to cut circular cathodes with diameters of 12.7 mm for half cells or 14.3 mm for full cells. For pouch cells, the cathodes were cut to 3.0 cm × 4.0 cm, with an additional tab for attaching to the leads.

Anode slurries were prepared by dispersing 95% Imerys GHDR Graphite, 1% carbon black, 1.25% carboxymethyl cellulose (CMC), 0.25% sodium lauryl sulfate (Soteras), and 2.5% styrene butadiene rubber (SBR) in deionized water. Trace oxalic acid was added to etch the current collector and improve adhesion. A doctor blade was used to coat the dispersion evenly on copper foil. A nominal loading of ~2.2 mA h cm^{-2} (6.3 mg cm^{-2}) or ~5 mA h cm^{-2} (14.2 mg cm^{-2}) was selected by varying the doctor blade height setting. The graphite electrodes were dried in an 80 °C oven and calendered in room-temperature rollers to a density ~1.3 g cm^{-3}.

Electrochemical analyses

Coin cell assembly was carried out inside an argon-filled glovebox. Cathode half-cells were assembled in CR2032 stainless steel coin-type cell cases. The working electrode was a 12.7 mm diameter disc punched from the NMC811 electrode described above, the separator was a 19 mm disc of layered polypropylene/polyethylene (Celgard 2325), and the counter electrode was a 450 μm lithium disc with 15 mm diameter. Full cells were assembled in CR2032 stainless steel coin-type cell cases (Hohsen), with a 14.3 mm cathode disc and 15.8 mm anode disc.

Pouch cells utilized a 3.0 cm × 4.0 cm cathode, and 3.1 cm × 4.1 cm anode. The electrodes were paired and wrapped with Celgard 2325 separator such that a single layer of separator was between the electrodes. Each electrode included an additional tab (from which active material was scraped off) to which the lead was affixed with an ultrasonic spot welder. The electrode stacks were then heat-sealed inside pouches consisting of polymer-coated aluminum foil, with one edge left open to add electrolyte. The cells were flooded with 400 μL electrolyte inside an argon-filled glovebox, and then transferred to a vacuum sealer in plastic bags to minimize air exposure. Lastly, the sealed cells were clamped between acrylic plates to maintain uniform stack pressure.

Electrochemical cycling tests were carried out on Arbin battery cyclers. The specific cycling conditions for each test are described in the Results section. Impedance spectra were collected on Biologic VMP3 and VMP300 potentiostats, and fitting was performed in python with the open-source library impedance.py.[31] The spectra were measured between 100 kHz and 100 mHz with 10 mV perturbation amplitude.

Materials characterization

XPS analysis was performed with a Versaprobe 4 X-ray photoelectron spectrometer. After cycling, the Swagelok cells were disassembled in an argon-filled glovebox and the graphite electrodes were harvested. After rinsing the electrode surfaces with dimethyl carbonate, small samples were cut from the center of each electrode and adhered to an XPS sample holder with double-sided conductive carbon tape. An airtight sample transfer vessel was used to transport the prepared samples from the glovebox to the XPS instrument, where the samples were drawn under vacuum without exposure to air. Fitting and analyses of the resulting data were performed in CasaXPS. SEM images and EDS maps were obtained with a Tescan Vega SEM operating at 20 kV, using the secondary electron detector. X-ray diffraction was carried out with a Rigaku Miniflex 600 instrument with a Cu Kα target (λ = 1.5406 Å). Scans were performed at 2θ = 10°–80° with 0.02° intervals.

Results and discussion

Impacts of formation rate on cathodes

In order to understand the impacts of increased formation rate on the behavior of LIB full-cells, it is critical to address the resilience of individual electrodes to fast formation rates. To confirm that the graphite anode is primarily responsible for capacity loss in the full cell in response to increased formation

rates, it is necessary to demonstrate that the impact of high formation rates on the cathode is negligible. NMC811 was synthesized as described in the Experimental section, and the diffraction pattern was confirmed to match with the $R\bar{3}m$ space group, as shown in Fig. S1.† The as-synthesized NMC811 exhibits ~10 μm secondary particles with spherical morphology, as shown in Fig. S2a,† and a uniform distribution of nickel, manganese, and cobalt, as shown by the energy dispersive X-ray spectroscopy (EDS) maps in Fig. S2b.† Lithium metal|NMC811 half-cells were formed with two different protocols and tested, as shown in Fig. 1. The first was a "standard" formation protocol consisting of constant-current (CC) cycles at C/10 rate (1C = 180 mA g^{-1}), shown in Fig. 1a. The second protocol consisted of constant-potential (CP) holds at the upper-cutoff potential (4.40 V) and then at lower cutoff potential (2.80 V) until the magnitude of current fell below a threshold rate of C/20, for three cycles, shown in Fig. 1b. Notably, the duration of formation cycles with the CP formation protocol is roughly an order of magnitude shorter than that with the CC protocol. Cells formed with both protocols were then subjected to a single cycle at C/10 rate to compare the irreversible capacity loss, followed by a constant-potential discharge from a fully charged state to compare rate capability.

During a potential hold, the current is initially limited by the rate of ion transport through the electrolyte (*i.e.*, diffusion-limited current),[32] and quickly decays to lower magnitudes, which are constrained by interfacial charge-transfer and electrode-level diffusion kinetics.[33] The quantitative current response depends strongly on the characteristics of the electrolyte, electrodes, and cell.[34] Thus, by completing formation through a series of potential holds, the cell and electrode materials are subjected to the maximum possible rate and shortest formation time. This comparison is designed to elucidate the response of the cathode under the limiting case of fast formation.

The potential profiles in Fig. 1c show that even when the cathode is subjected to the maximum formation rate during CP formation, no additional irreversible capacity loss is incurred compared to CC formation. Actually, the cells that underwent CP formation exhibit significantly higher capacity, but this difference is largely attributed to the lithium–metal anode, whose increased surface area after plating and stripping at high current density can dramatically reduce the internal resistance of the half-cell. Additionally, a constant-potential discharge was performed to obtain a rate capability profile, shown in Fig. 1d. Both formation protocols yield similar rate capability up to a rate of ~2C. Beyond this rate, the rate capability is dominantly determined by ion-transport characteristics within the porous electrode,[33,35] and therefore varies due to slight variations in electrode loading between cells.

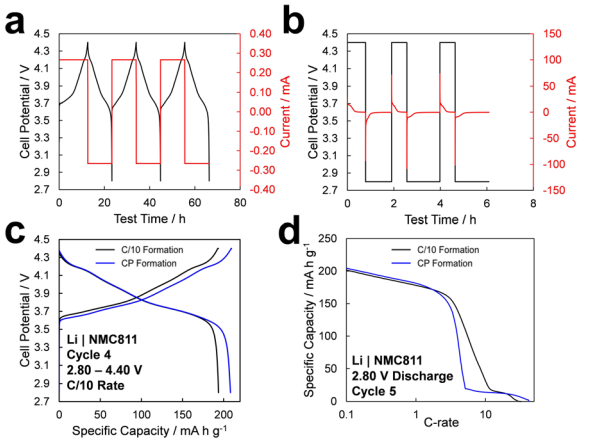

Fig. 1 Effects of fast formation on NMC811 half-cells. Potential (black) and current (red) *vs.* time profiles corresponding to (a) constant-current (CC) formation at C/10 rate and (b) constant-potential (CP) formation. (c) Potential *vs.* capacity profiles during galvanostatic operation at C/10 rate and (d) discharge rate capability profile during constant-potential operation after formation cycles are completed with different protocols.

Impacts of formation rate on graphite SEI formation

The results shown in Fig. 1 demonstrate that fast formation conditions do not degrade the performance of NMC811. This confirms that in LIB full cells, it is the graphite anode that largely limits the formation rate. Therefore, we sought to more closely investigate the dependence of the anode SEI characteristics on the formation rate. Graphite|NMC811 Swagelok cells were constructed with LP57 electrolyte. Each cell was subjected to a single formation cycle at a rate of C/10, C/2, or 1C. The potential *versus* time profiles are shown in Fig. S3a,† and potential *versus* capacity profiles are shown in Fig. S3b,† for each formation rate.

After the formation cycles were completed at different rates, the Swagelok cells were disassembled and the formed anodes were harvested for analysis with X-ray photoelectron spectroscopy (XPS). The corresponding carbon, oxygen, and fluorine region scans are shown, respectively, in Fig. 2a, b and c. In the C 1s spectra, the C–C peak becomes relatively weaker with increased formation rate, indicating a weakening of the graphitic signal. The O 1s spectra indicate increased prevalence of C–O groups, consistent with solvent reduction products, which is confirmed by the C–O and C=O peaks in the C 1s spectra. The F 1s spectra indicate that as the formation rate increases, Li–F is formed preferentially compared to $LiPF_6$ and its decomposition products.[24,30,36–38] The elemental proportions from survey scans are shown in Fig. 2d as a function of formation rate. The ratios of C, O, and F remain relatively similar at C/10 and C/2 rates, but the proportion of oxygen increases significantly during 1C formation, suggesting an increased prevalence of solvent reduction products in the SEI.

Recognizing that the potential for lithium–metal deposition presents a serious limitation to the practical formation rate, we chose to repeat this experiment with a second electrolyte: a localized high-concentration electrolyte (LHCE) consisting of 1.50 M lithium bis(fluorosulfonyl)imide (LiFSI) in fluoroethylene carbonate (FEC) and dimethyl carbonate (DMC) with 2,2,2-trifluoroethyl, 1,1,2,2 tetrafluoropropyl ether (TTEE). The exact

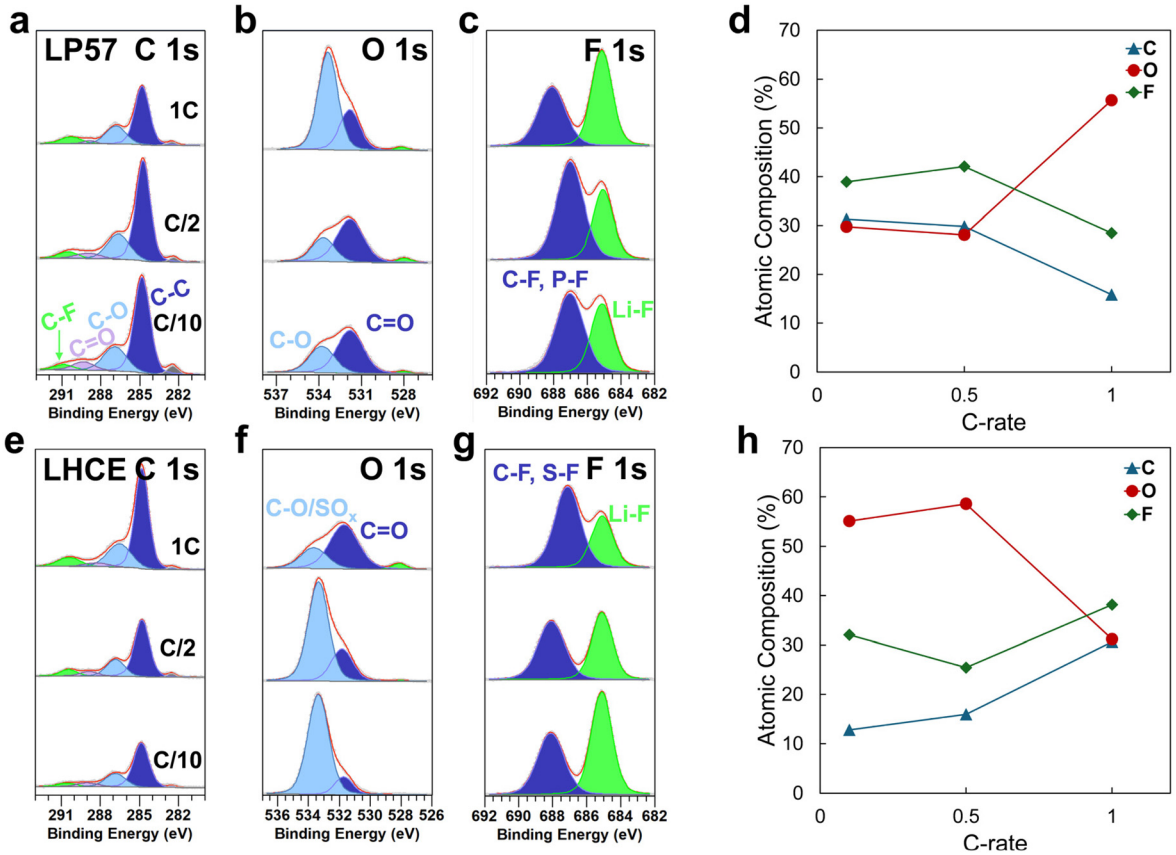

Fig. 2 XPS Analyses of Electrodes formed at different rates in LP57 and LHCE electrolytes. (a) C 1s, (b) O 1s, and (c) F 1s spectra of graphite electrodes after forming at rates of C/10 (bottom), C/2 (middle), and 1C (top) with LP57 electrolyte. (d) Elemental proportions of C, O, and F with LP57 as formation rate is increased. (e) C 1s, (f) O 1s, and (g) F 1s spectra after forming with LHCE. (h) Elemental proportions of C, O, and F with LHCE as formation rate is increased.

composition of this electrolyte is specified in the Experimental section and in our previous work.[29] Importantly, our previous work with this electrolyte has highlighted its ability to suppress irreversible lithium plating by forming an SEI which allows facile charge-transfer at the anode interface.[29]

The potential *versus* time and potential *versus* capacity profiles for the formation cycles of the graphite|NMC811 Swagelok cells with LHCE are shown in, respectively, Fig. S4a and S4b.† Notably, as the formation rate is increased, the LHCE yields higher coulombic efficiency than the LP57. This suggests that at high formation rates, the LHCE forms a less resistive interphase, reducing ohmic capacity losses, and/or reduces lithium inventory loss during SEI formation, resulting in higher discharge capacity.

The carbon, oxygen, and fluorine region scans and elemental proportions with the LHCE are show in, respectively, Fig. 2e, f, g and h. Interestingly, the trends in the SEI composition with increasing formation rate are generally opposite to those observed with LP57: stronger graphitic peak in the C 1s region, greater prevalence of C═O compared to C–O in the O 1s region, and greater prevalence of salt decomposition products compared to Li–F in the F 1s region. From Fig. 2h, it is clear that the overall trends in carbon, oxygen, and fluorine content with increasing formation rate are opposite to those observed for LP57 in Fig. 2d. This implies that as the formation rate is increased with LHCE electrolyte, the anode SEI becomes thinner, and is composed of less solvent-derived and more inorganic/salt-derived species. Our previous work demonstrates that the reduced propensity for lithium metal deposition associated with the LHCE is primarily a result of the use of LiFSI salt, rather than the differences in solvent or solvation structure.[29]

Additional XPS spectra were collected after 60 s of argon sputtering, shown in Fig. S5 and S6† for, respectively, LP57 and LHCE. For each sample, the graphitic signal is proportionally stronger after sputtering, confirming that the SEI is thinner. In the O 1s region, the C–O signal becomes weaker and C═O signal becomes stronger after sputtering, suggesting that the region of the SEI closer to the electrode is composed of more inorganic species (*e.g.*, Li_2CO_3). This is confirmed by the F 1s region, which shows a shift toward stronger LiF signal after sputtering. These results demonstrate that for all of the samples examined, the inner SEI region is relatively rich in inorganic species compared to the region further from the electrode, which is consistent with the findings in previous work.[39]

Pouch full cell testing with different formation rates

Given the demonstrated potential of the LHCE with LiFSI salt to facilitate faster formation rates without significant penalties to safety and reversible capacity, extended cycling tests were carried out in graphite|NMC811 pouch full cells under different formation protocols. The results of these tests are shown in Fig. 3. A detailed description of pouch cell electrode preparation and assembly is provided in the Experimental section.

A comparison of pouch full cells formed at different rates with LP57 is shown in Fig. 3a. After three formation cycles, the cells were cycled at 1C rate with periodic capacity checks at C/10 and C/3. The behavior is very similar between the pouch cells formed at C/10, C/2 and 1C rates, with 1C formation yielding slightly higher capacity retention than C/2 or C/10 formation. Another test was conducted in which the formation was carried out at constant potential, labeled as CP. Throughout the formation charge, a 4.25 V cell potential was maintained, and for discharge a 2.50 V potential was maintained, for three formation cycles. The charge/discharge step was terminated when the current magnitude fell below a threshold rate of C/20. Clearly, this aggressive formation condition leads to a dramatic loss of capacity, both during 1C cycling and C/10 capacity checks. Moreover, it is noted that one of these pouch cells completely short-circuited during the first constant-potential charge, which is likely due to a lithium dendrite penetrating the separator.

The potential profiles of the 1st cycle for each formation protocol are shown in Fig. 3b, with a table indicating the first cycle duration for each formation protocol. As expected, the higher formation rates markedly reduce the duration, and a duration of ~2.9 h can be realized without irreversible capacity loss. The potential profiles of the 100th 1C discharge and subsequent C/10 discharge with LP57 electrolyte are shown in Fig. 3c. The cells formed with rates of C/10–1C exhibit very similar potential profiles at 1C and C/10 rates. The similar potential polarization between different formation rates illustrates that formation rates up to 1C do not significantly increase the internal resistance of cell—an observation which is corroborated by the progression of impedance data, shown in Fig. S7a and S8a.† Even after formation at constant potential, which incurs a significant irreversible loss of capacity, the charge-transfer resistance does not increase—rather, slightly decreases—with cycle life. Furthermore, the potential curves shown in Fig. 3c for CP formation do not diverge from those of the other formation protocols until a discharge capacity of 50–75 mA h g^{-1} is reached. These observations strongly indicate that the capacity loss resulting from CP formation is mainly a result of irreversible loss of lithium inventory, rather than increasing resistance of the SEI or CEI.

For the pouch full cells utilizing LHCE electrolyte, the cycling results are shown in Fig. 3d. Similar to the cells with LP57 electrolyte, there is very little difference in performance between the cells formed at C/10, C/2, or 1C rate, with each delivering marginally higher discharge capacity than the cells with LP57 electrolyte. However, under the constant-potential formation protocol, the result is markedly different from that observed with LP57 electrolyte, with no significant capacity

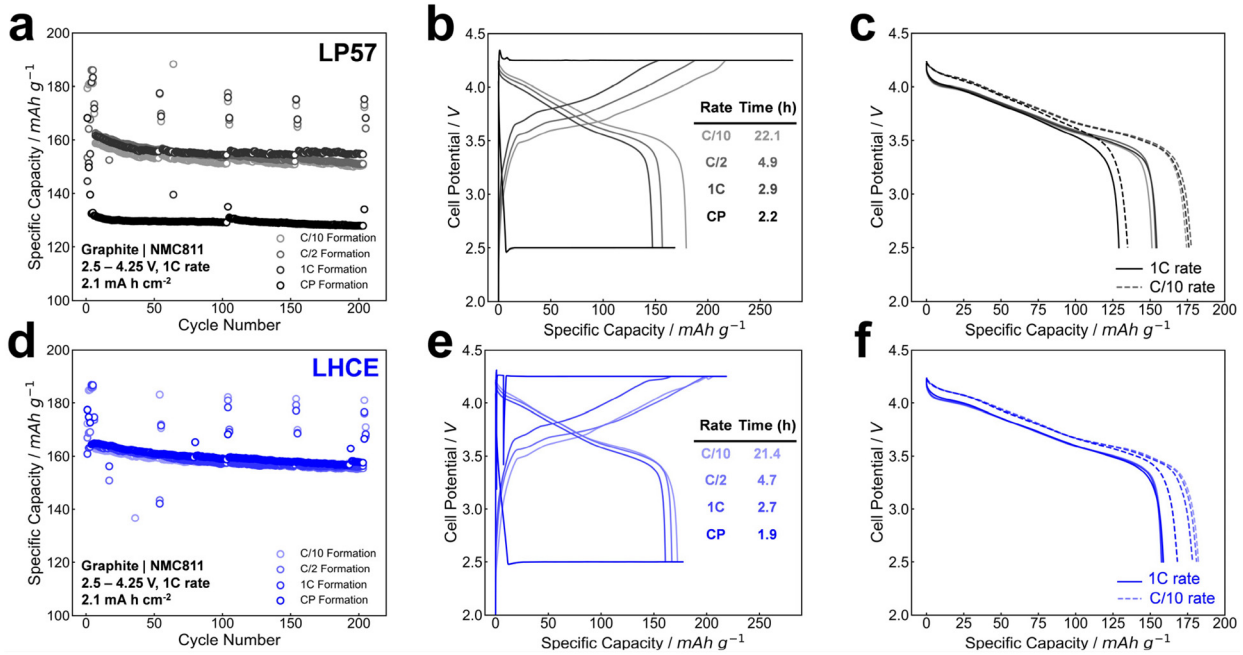

Fig. 3 Electrochemical cycling of graphite|NMC811 pouch cells with different formation protocols. (a) Extended cycling tests with formation at different rates, (b) first-cycle potential profiles at different rates, and (c) 1C and C/10 discharge potential profiles after 100 cycles with formation at different rates with LP57 electrolyte. (d) Extended cycling tests, (e) first-cycle potential profiles, and (f) 1C and C/10 discharge potential profiles after 100 cycles with LHCE electrolyte.

difference observed with respect to the other formation rates during 1C cycling. The potential profiles of the 1st cycle for each formation rate are shown in Fig. 3e, with a table indicating the duration of each formation cycle. The results show that, with LHCE electrolyte, the 1st cycle can be completed in ~1.9 h without irreversible loss of capacity at 1C rate. Fig. 3f shows the potential profiles from the 100th 1C discharge and subsequent C/10 discharge. The potential profiles are well aligned at 1C rate for each formation protocol. At C/10 rate, the potential profiles are well aligned for C/10 to 1C formation protocols, but CP formation results in significant capacity loss. Similar to the case for LP57 shown in Fig. 3c, the alignment of the potential profiles suggests that this loss of capacity is primarily due to loss of lithium inventory. Interestingly, the charge-transfer resistance appears to increase monotonically with cycle life for the cells with LHCE electrolyte, a behavior which is not manifested with the LP57 electrolyte. Notably, however, when using the LHCE electrolyte, the charge-transfer resistance decreases with increasing formation cycle rate. These observations are shown in Fig. S7b and S8b.†

Coulombic efficiency values throughout cycling are presented in Fig. S9† for both electrolytes. As shown in Fig. S9a† for the LP57 cells, the coulombic efficiency stabilizes at ~100% for formation rates from C/10 to 1C. For CP formation, the coulombic efficiency stabilizes at a value significantly above 100%, which is likely because a portion of lithium–metal deposited during the formation cycles remains electrochemically accessible, serving as a lithium reservoir. For the LHCE cells, shown in Fig. S9b,† a very similar trend is observed.

To properly assess the viability of increasing the formation rate, it is important to compare the resulting cell performance on the basis of energy density, rather than only specific capacity. Thus, the energy densities of the final discharges at 1C and C/10 rates for each test are presented in Table S1.† Interestingly, cells with LP57 electrolyte deliver slightly higher energy density as the formation rate is increased from C/10 to 1C. However, in the case of constant potential formation, the energy density drops dramatically. For LHCE electrolyte, the energy density delivered by cells formed from C/10 to 1C decreases slightly at C/10 rate, but is similar at 1C rate, suggesting that this difference may be attributed to irreversible lithium inventory loss. In the case of constant potential formation with LHCE electrolyte, the energy density drops somewhat at C/10 rate compared to slower formation rates, but the retention is still markedly better than with LP57 electrolyte. At 1C rate, constant potential formation does not incur any loss of energy density. Notably, cells with LHCE electrolyte deliver higher energy density than the corresponding cells with LP57 electrolyte across all test conditions examined.

Postmortem analyses of pouch cells

After cycling, the pouch cells formed at different rates were discharged at 1C rate to a 2.50 V cutoff, and then charged at a 1C rate for 20 minutes to bring the electrodes to a medium SOC. The cells were then brought into an argon-filled glovebox and disassembled. Samples were obtained from the cycled electrodes for postmortem imaging and electrochemical analyses.

Images of the recovered graphite anodes from cells with LP57 electrolyte are shown in Fig. S10a,† revealing a clear correlation between the formation rate and the severity of lithium–metal deposition. The corresponding images for LHCE, shown in Fig. S10b,† manifest less severe lithium plating. Also, the color of the graphite anodes formed in LHCE indicate a higher degree of lithiation than the corresponding anodes formed in LP57. Since the cells were charged to the same specific capacity before disassembly, this indicates that the degree of lithiation was lower for the anodes with LP57 electrolyte than those with LHCE after the final discharge.

Cross-sectional scanning electron microscopy (SEM) images were obtained from the lithium-plated regions of CP-formed anodes, shown in Fig. 4. Interestingly, the morphologies of lithium deposition are markedly different between the two electrolytes: LP57 yields a highly dendritic and porous plating morphology in a thick (~40–50 μm) layer (Fig. 4a), while LHCE yields a more compact (~10 μm) layer (Fig. 4b). This observation is consistent with previous findings comparing the lithium-deposition morphology between $LiPF_6$ and LiFSI salts.[40] Various EDS elemental maps are shown for LP57 in Fig. 4c. These clearly differentiate the compositions of current collector, graphite particles, and deposited lithium regions shown in Fig. 4a. The thick lithium plated region is rich in fluorine, oxygen, and phosphorus, which may be ascribed to reaction products from the PF_6^- polyanion and lithium metal with the carbonate solvent. The EDS maps for LHCE are shown in Fig. 4d, confirming that the deposited lithium

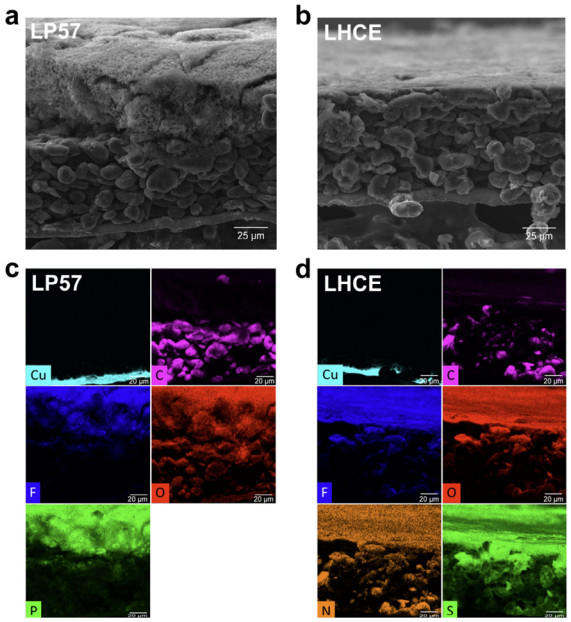

Fig. 4 Cross-sectional SEM images of lithium-plated regions from pouch cell electrodes cycled with (a) LP57 and (b) LHCE electrolyte. EDS maps of various elemental distributions from (c) LP57 and (d) LHCE SEM images.

region is a compact layer uniformly coating the surface of the electrode, and is rich in FSI^- and lithium–metal reaction products. SEM images are presented in Fig. S11,† showing the surface morphologies of the cycled graphite particles and metallic lithium deposition. Notably, the morphology of lithium–metal deposition with LHCE is both more compact and less dendritic than with LP57, likely due to the differences in salt and solvation structures.[41] This may assuage concerns regarding the possibility of lithium dendrites penetrating the separator.

Half-cells were assembled with the cycled cathode material, comprised of lithium–metal counter electrodes, cycled NMC811 cathodes, and the same electrolytes as used in the pouch cells from which the cathodes were harvested. The half-cells were first discharged at C/10 rate to 2.80 V, shown for LP57 in Fig. 5a. The results show a significant difference in discharge capacity, with the cathode formed at constant potential delivering the highest discharge capacity. This indicates that at the discharged state in the full cell (after discharging to 2.50 V), this cathode had a lower degree of lithiation than those formed at lower rates (C/10 to 1C), which corresponds to a larger inventory of lithium on the anode side, either intercalated in or plated on graphite anode. In turn, the lower first discharge capacities of the cathodes formed at lower rates indicates less lithium inventory remaining on the anode side after the final discharge.

After the initial discharge, the half-cells were subjected to a full cycle at C/10 rate, with an upper cutoff potential of 4.40 V and lower cutoff potential of 2.80 V, shown in Fig. 5b. With a practically unlimited lithium reservoir in the counter electrode, the cell capacity is limited only by the NMC811 working electrode, so the capacity reflects the total reversible capacity of the cycled cathode. Even after 200 cycles in pouch full cells, the cathodes formed at different rates have very similar potential profiles and deliver >200 mA h g^{-1} on discharge. This confirms that there is no significant loss of active material on the cathode side after the 200-cycle test, and corroborates the results shown in Fig. 1 that the cathode does not suffer irreversible capacity loss due to increased formation rates.

Symmetric cells were assembled with two electrode discs from each cycled graphite anode, and shorted for 15 minutes. The charge-transfer activation energy was measured by collecting impedance spectra of the symmetric cells at various temperatures (0 °C–40 °C), as shown in the Arrhenius plots in Fig. 5c. The charge-transfer activation energy increases significantly with the formation C-rate, which as shown in our previous work, indicates a higher propensity for lithium metal plating.[29] The impedance spectra and fits are shown in Fig. S12.† The corresponding electrochemical tests for LHCE electrolyte are shown in Fig. 5d–f. During the initial half-cell discharge test (Fig. 5d), all cathodes deliver similar discharge capacity, indicating that a similar proportion of lithium is retained on the anode side. By comparing the colors of cycled graphite electrodes in Fig. S10,† it is clear that for the cells cycled with LP57 electrolyte, a greater proportion of this lithium is deposited in metallic form on the electrode surface, whereas for those cycled with LHCE electrolyte, a greater proportion is intercalated into the graphite. This is quantitatively

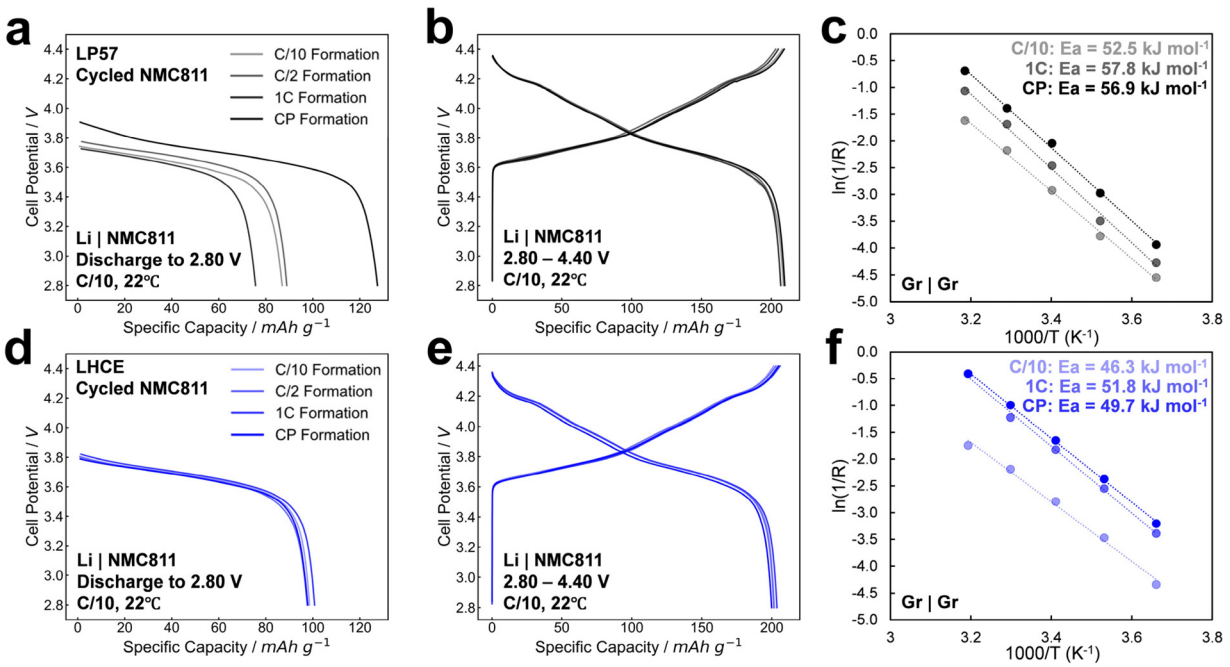

Fig. 5 Post-mortem electrochemical analyses of graphite|NMC811 pouch cells. (a) First discharge and (b) full C/10 cycle of cycled NMC811 half cells in LP57 electrolyte. (c) Arrhenius activation energy measurements for cycled graphite electrodes after C/10, 1C, and CP formation and cycling in LP57 electrolyte. (d) First discharge and (e) full C/10 cycle of cycled NMC811 half cells in LHCE electrolyte. (f) Arrhenius activation energy measurements for cycled graphite electrodes after C/10, 1C, and CP formation and cycling in LHCE electrolyte.

confirmed by Fig. S13,† which compares the accessible lithium inventory remaining in the graphite electrode after cell disassembly. The higher first-charge capacities of graphite half cells from LHCE pouch cells (Fig. S13b†) indicate larger accessible lithium inventory than from LP57 pouch cells (Fig. S13a†).

The potential profiles shown in Fig. 5e demonstrate that, similar to the case for the cycled LP57 electrodes shown in Fig. 5b, the reversible capacity of the cathodes remains ≥200 mA h g^{-1} and is similar between different formation rates. From the Arrhenius test data shown in Fig. 5f, the anodes cycled with LHCE appear to exhibit higher charge-transfer activation energy with increased formation rate, similar to those cycled in LP57. However, the activation energies from the LHCE electrolyte remain lower than those from the LP57 electrolyte, consistent with our previous findings.[29] This finding demonstrates the resilience of the SEI formed by the LHCE electrolyte to lithium metal deposition, compared to the LP57 electrolyte.

Full cell testing with high active material loading

While the constant-potential formation protocol used in the above pouch cell tests is effective for elucidating the potential impacts of high formation rates and their dependence on the electrolyte, it is not tenable for practical applications, due in part to the large current magnitude required during the initial charge/discharge. Moreover, the critical current density required to induce lithium–metal deposition depends strongly on the thickness of the porous electrode material.[42] Consequently, although the pouch cell tests shown in Fig. 3 ostensibly imply that LIBs can tolerate formation rates up to 1C without loss of performance, this may not accurately represent the behavior of practical LIB electrodes, which often have much higher loading (5–6 mA h cm^{-2}), due to the more significant impacts of sluggish ion transport in the porous electrodes. Thus, to evaluate a system that more closely represents a practical condition, NMC811 cathodes with higher loading (~4.5 mA h cm^{-2}) were prepared with an active material : carbon black : PVDF weight ratio of 95 : 2.5 : 2.5. Graphite anodes were prepared with ~5 mA h cm^{-2} loading for an N/P areal capacity ratio of ~1.06. Coin full cells were prepared with the LP57 and LHCE electrolytes and tested under different formation conditions, as shown in Fig. 6.

The electrochemical cycling behavior of high-loading cells with LP57 electrolyte is shown in Fig. 6a. Evidently, the cells formed at 1C rate experience a precipitous loss of capacity within the first ~10 cycles compared to those formed at C/10. Potential profiles from the final C/10 cycles are shown in Fig. 6b, demonstrating that the capacity loss can be primarily attributed to loss of lithium inventory. This comparison is markedly different for the cells formed at C/10 and 1C with LHCE, as shown in Fig. 6c. In this case, there is no loss of capacity at 1C rate resulting from increased formation rate. The final C/10 rate potential profiles shown in Fig. 6d confirm that there is some loss of reversible capacity due to lithium inventory loss, but to a far lesser extent than was observed in Fig. 6b.

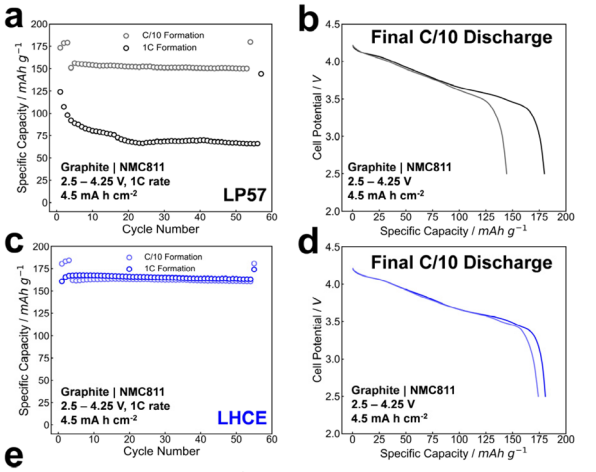

e

Electrolyte	Formation C-rate	1st cycle duration (h)	1C energy density (W h kg^{-1})	C/10 energy density (W h kg^{-1})
LP57	C/10	22.0	534	667
LP57	1C	3.6	240	533
LHCE	C/10	22.2	576	672
LHCE	1C	2.7	547	622

Fig. 6 Electrochemical cycling and performance comparison of graphite|NMC811 coin cells with high electrode loading. (a) Electrochemical cycling tests with formation at C/10 and 1C rates in LP57 electrolyte. (b) C/10 discharge potential profiles after 50 cycles at 1C rate. (c) Electrochemical cycling tests with formation at C10 and 1C rates and (d) C/10 discharge potential profiles after 1C cycling with LHCE electrolyte. (e) Table of first cycle duration and energy density for each test condition.

To facilitate quantitative comparison, Fig. 6e presents a table summarizing the key performance metrics. Compared to slow C/10 formation, 1C formation yields some irreversible capacity loss for either electrolyte. However, the LHCE electrolyte greatly mitigates this phenomenon, to the extent that even after forming at 1C rate, the full cells still deliver higher energy density at 1C rate than those formed with LP57 electrolyte at a slow C/10 rate. Thus, for certain applications, the formation time may be reduced to ~3 h, even with thick electrodes. Images of the cycled graphite electrodes are shown in Fig. S14† to compare the extent of lithium plating. These analyses demonstrate that with practically relevant cell design parameters (*i.e.*, high loading), 1C formation is indeed sufficient to induce severe capacity loss with conventional electrolytes due to loss of lithium inventory. However, an electrolyte which is effective in suppressing irreversible lithium plating can largely mitigate this problem.

When the formation rate is increased to a value that incurs significant lithium plating, it is inevitable that some irreversible loss of capacity will result in LIBs due to lithium inventory loss. However, the manifestation of this loss is rate-dependent, overshadowed by electrode kinetic limitations at higher C-rates. By engineering an SEI which offers more facile charge-transfer kinetics, favoring the intercalation of lithium over deposition on the graphite surface, this irreversible capacity

loss can be greatly suppressed. Herein, we have demonstrated this with an LHCE containing LiFSI salt. This electrolyte does not entirely prevent lithium–metal deposition, but dramatically alters its morphology, yielding a compact layer, which minimizes lithium inventory loss and improves safety.

Electrode thickness, porosity, and tortuosity also play a critical role in mediating ion transport in porous electrodes and in turn, determining the severity of lithium plating for a given set of operating conditions. This relationship is of critical importance when considering the prospects for fast formation in practical LIBs, such as those for automotive applications.[43] Our work has clearly demonstrated that a "conventional" electrolyte, such as LP57, can support high formation rates when the electrode loading is of a typical value used in research (~2.1 mA h cm^{-2}), but the same formation rate is not feasible when the loading is of a typical value used in industry. As a result, previous findings demonstrating short formation times with low loadings may not translate well to large-scale applications, which demand high electrode loading and press density to maximize energy density.

The rate of ion transport within the porous electrode also depends on the transport properties of the electrolyte. Here, we focused on the role of the electrolyte on mediating interfacial phenomena including lithium plating and SEI formation. However, LHCEs generally exhibit significantly lower ionic conductivity than conventional electrolytes like LP57, due to the impacts of ion dissociation and mobility. Thus, investigating the interplay between SEI formation and electrolyte transport properties would be a valuable future research direction in the pursuit of reducing formation time.

It is apparent from the results shown above that strategic electrolyte design, principally involving the partial or complete substitution of $LiPF_6$ salt with LiFSI, can provide a pathway toward faster formation of LIBs. As one of the most expensive and energy-intensive steps of LIB manufacturing, the formation process represents a crucial bottleneck. Although the high cost of LiFSI salt is often cited as one of its main disadvantages,[44] the potential for reducing formation time and energy may offset this.

Conclusions

The work explored the potential for fast formation rates in LIB full cells. It is demonstrated that whereas the NMC811 cathode can readily tolerate rapid formation rates without irreversible degradation, it is the susceptibility of the graphite anode to lithium–metal deposition, which most severely constrains the formation rate. Our electrochemical tests on cells with different areal loadings clearly show that this phenomenon depends strongly on the electrode thickness as well as on the formation rate. Our work addresses this dependence, showing that at more practical electrode loadings that were used in previous work, the maximum tenable formation rate is indeed much lower than that at the medium or low electrode loadings often used in research. However, for the inverse trend, it is demonstrated that formation rates up to 1C are tolerated when lower electrode loadings (~2 mA h cm^{-2}) are used, which could allow faster experimental throughput (*e.g.*, in lab-scale research).

By employing an electrolyte that effectively suppresses irreversible lithium plating (as shown in our previous work),[29] the tolerance for fast formation is profoundly improved. This is due to the formation of an SEI whose structure and composition enable facile and rapid charge-transfer into the electrode, ameliorating irreversible lithium–metal deposition. Despite the high cost of LiFSI salt in comparison to $LiPF_6$, it may be offset by the potential for reduced formation time, as formation is one of the most expensive steps in the LIB manufacturing process.[45] Overall, our work explored the limits of formation rate and its interplay with electrode loading, and introduced an electrolyte design strategy for extending these limits. The findings outlined herein are of great value to the advancement of LIB manufacturing throughput, in both lab and industrial settings.

Author contributions

S. O. developed the project idea and methodology, and carried out all experimental analyses. A. M. supervised the research.

Data availability

All the data associated with the findings presented in this study are available within this article and its ESI.†

Conflicts of interest

There are no conflicts to declare.

Acknowledgements

This work was supported by the Welch Foundation grand F-1254. The first author (S. O.) was supported by the National Science Foundation Graduate Research Fellowship.

References

1 O. Catsaros, Lithium-Ion Battery Pack Prices Hit Record Low of $139/kWh, https://about.bnef.com/blog/lithium-ion-battery-pack-prices-hit-record-low-of-139-kwh/, (accessed 18 January 2025).
2 L. Mauler, F. Duffner, W. G. Zeier and J. Leker, *Energy Environ. Sci.*, 2021, **14**, 4712–4739.
3 L. Usai, J. J. Lamb, E. Hertwich, O. S. Burheim and A. H. Strømman, *Environ. Res.: Infrastruct. Sustainability*, 2022, **2**, 011002.

4 Y. Liu, R. Zhang, J. Wang and Y. Wang, *iScience*, 2021, **24**, 102332.
5 H. H. Heimes, A. Kampker, C. Lienemann, M. Locke, C. Offermanns, S. Michaelis and E. Rahimzei, *Lithium-ion battery cell production process*, PEM der RWTH Aachen University, Aachen, 2018.
6 F. Degen, M. Winter, D. Bendig and J. Tübke, *Nat. Energy*, 2023, **8**, 1284–1295.
7 D. L. Wood, J. Li and C. Daniel, *J. Power Sources*, 2015, **275**, 234–242.
8 F. Duffner, L. Mauler, M. Wentker, J. Leker and M. Winter, *Int. J. Prod. Econ.*, 2021, **232**, 107982.
9 J. Li, Z. Du, R. E. Ruther, S. J. An, L. A. David, K. Hays, M. Wood, N. D. Phillip, Y. Sheng, C. Mao, S. Kalnaus, C. Daniel and D. L. Wood, *JOM*, 2017, **69**, 1484–1496.
10 F. Schomburg, B. Heidrich, S. Wennemar, R. Drees, T. Roth, M. Kurrat, H. Heimes, A. Jossen, M. Winter, J. Y. Cheong and F. Röder, *Energy Environ. Sci.*, 2024, **17**, 2686–2733.
11 D. L. Wood, J. Li and S. J. An, *Joule*, 2019, **3**, 2884–2888.
12 Q. Liu, C. Du, B. Shen, P. Zuo, X. Cheng, Y. Ma, G. Yin and Y. Gao, *RSC Adv.*, 2016, **6**, 88683–88700.
13 D. P. Finegan, A. Quinn, D. S. Wragg, A. M. Colclasure, X. Lu, C. Tan, T. M. M. Heenan, R. Jervis, D. J. L. Brett, S. Das, T. Gao, D. A. Cogswell, M. Z. Bazant, M. D. Michiel, S. Checchia, P. R. Shearing and K. Smith, *Energy Environ. Sci.*, 2020, **13**, 2570–2584.
14 X. Lin, K. Khosravinia, X. Hu, J. Li and W. Lu, *Prog. Energy Combust. Sci.*, 2021, **87**, 100953.
15 S. Xu, K.-H. Chen, N. P. Dasgupta, J. B. Siegel and A. G. Stefanopoulou, *J. Electrochem. Soc.*, 2019, **166**, A3456.
16 K. S. N. Vikrant, E. McShane, A. M. Colclasure, B. D. McCloskey and S. Allu, *J. Electrochem. Soc.*, 2022, **169**, 040520.
17 S. J. An, J. Li, C. Daniel, D. Mohanty, S. Nagpure and D. L. Wood, *Carbon*, 2016, **105**, 52–76.
18 S. J. An, J. Li, Z. Du, C. Daniel and D. L. Wood, *J. Power Sources*, 2017, **342**, 846–852.
19 H.-H. Lee, Y.-Y. Wang, C.-C. Wan, M.-H. Yang, H.-C. Wu and D.-T. Shieh, *J. Power Sources*, 2004, **134**, 118–123.
20 Z. Guo, Z. Cui and A. Manthiram, *ACS Energy Lett.*, 2024, **9**, 3316–3323.
21 C. Mao, S. J. An, H. M. Meyer, J. Li, M. Wood, R. E. Ruther and D. L. Wood, *J. Power Sources*, 2018, **402**, 107–115.
22 H. H. Heimes, C. Offermanns, A. Mohsseni, H. Laufen, U. Westerhoff, L. Hoffmann, P. Niehoff, M. Kurrat, M. Winter and A. Kampker, *Energy Technol.*, 2020, **8**, 1900118.
23 R. Drees, F. Lienesch and M. Kurrat, *J. Energy Storage*, 2021, **36**, 102345.
24 S. M. Oh, J. Song, S. Lee and I.-C. Jang, *Electrochim. Acta*, 2021, **397**, 139269.
25 B. K. Antonopoulos, C. Stock, F. Maglia and H. E. Hoster, *Electrochim. Acta*, 2018, **269**, 331–339.
26 R. Drees, F. Lienesch and M. Kurrat, *Energy Technol.*, 2023, **11**, 2200868.
27 S. Lei, Z. Zeng, S. Cheng and J. Xie, *Battery Energy*, 2023, **2**, 20230018.
28 C. Sun, X. Ji, S. Weng, R. Li, X. Huang, C. Zhu, X. Xiao, T. Deng, L. Fan, L. Chen, X. Wang, C. Wang and X. Fan, *Adv. Mater.*, 2022, **34**, 2206020.
29 S. Ober and A. Manthiram, *Small*, 2024, 2405731.
30 X. Yue, J. Zhang, Y. Dong, Y. Chen, Z. Shi, X. Xu, X. Li and Z. Liang, *Angew. Chem., Int. Ed.*, 2023, **62**, e202302285.
31 M. D. Murbach, B. Gerwe, N. Dawson-Elli and L. Tsui, *J. Open Source Software*, 2020, **5**, 2349.
32 C. Heubner, M. Schneider and A. Michaelis, *Adv. Energy Mater.*, 2020, **10**, 1902523.
33 R. Xiong, M. Zhou, L. Li, J. Xu, M. Li, B. Yan, D. Li, Y. Zhang and H. Zhou, *Energy Storage Mater.*, 2023, **54**, 836–844.
34 A. J. Bard, L. R. Faulkner and H. S. White, *Electrochemical Methods: Fundamentals and Applications*, John Wiley & Sons, 2022.
35 Y.-X. Yao, L. Xu, C. Yan and Q. Zhang, *EES Batteries*, 2025, **1**, 9–22.
36 M. Khasanov, E. Pazhetnov and W. C. Shin, *J. Electrochem. Soc.*, 2015, **162**, A1892.
37 L.-L. Jiang, C. Yan, Y.-X. Yao, W. Cai, J.-Q. Huang and Q. Zhang, *Angew. Chem., Int. Ed.*, 2021, **60**, 3402–3406.
38 S.-J. Kang, K. Park, S.-H. Park and H. Lee, *Electrochim. Acta*, 2018, **259**, 949–954.
39 H. Adenusi, G. A. Chass, S. Passerini, K. V. Tian and G. Chen, *Adv. Energy Mater.*, 2023, **13**, 2203307.
40 G. Yang, Y. Li, S. Liu, S. Zhang, Z. Wang and L. Chen, *Energy Storage Mater.*, 2019, **23**, 350–357.
41 Y. Chen, M. Li, Y. Liu, Y. Jie, W. Li, F. Huang, X. Li, Z. He, X. Ren, Y. Chen, X. Meng, T. Cheng, M. Gu, S. Jiao and R. Cao, *Nat. Commun.*, 2023, **14**, 2655.
42 A. M. Colclasure, T. R. Tanim, A. N. Jansen, S. E. Trask, A. R. Dunlop, B. J. Polzin, I. Bloom, D. Robertson, L. Flores, M. Evans, E. J. Dufek and K. Smith, *Electrochim. Acta*, 2020, **337**, 135854.
43 M. Ank, A. Sommer, K. Abo Gamra, J. Schöberl, M. Leeb, J. Schachtl, N. Streidel, S. Stock, M. Schreiber, P. Bilfinger, C. Allgäuer, P. Rosner, J. Hagemeister, M. Rößle, R. Daub and M. Lienkamp, *J. Electrochem. Soc.*, 2023, **170**, 120536.
44 S. Zhou, Y. Liu, F. Ren, S. Zhang, X. Shi, B. Wu, L. Yan, J. Chen and F. Zhang, *Sep. Purif. Technol.*, 2025, **362**, 131654.
45 Lithium ion battery costs: materials and manufacturing?, **https://thundersaidenergy.com/downloads/lithium-ion-batteries-for-electric-vehicles-what-costs/**, (accessed 13 October 2024).